THE ASTROPHYSICAL JOURNAL, 424:491–502, 1994 March 20

THE COSMIC-RAY ENERGY SPECTRUM OBSERVED BY THE FLY'S EYE

D. J. BIRD,[1] S. C. CORBATÓ,[2] H. Y. DAI,[2] B. R. DAWSON,[3] J. W. ELBERT,[2] B. L. EMERSON,[2,4] K. D. GREEN,[2,5] M. A. HUANG,[2] D. B. KIEDA,[2] M. LUO,[2] S. KO,[2] C. G. LARSEN,[2] E. C. LOH,[2] M. H. SALAMON,[2] J. D. SMITH,[2] P. SOKOLSKY,[2] P. SOMMERS,[2] J. K. K. TANG,[2] AND S. B. THOMAS[2]

Received 1993 August 16; accepted 1993 September 24

ABSTRACT

We report on the cosmic-ray energy spectrum above 10^{17} eV as observed by the Fly's Eye detector. The detector has been operated in monocular mode (Fly's Eye I only) since 1981 and in stereo mode (both Fly's Eye I and Fly's Eye II) since 1986. This paper includes data through 1992 July. The cosmic-ray primary energy is measured by integrating over the atmospheric development curve of the extensive air shower produced by the primary particle. The differential monocular energy spectrum above 10^{17} eV is $J(E) = 10^{-29.55} \times (E/10^{18}\ \mathrm{eV})^{-3.07\pm0.01}\ \mathrm{m}^{-2}\ \mathrm{s}^{-1}\ \mathrm{sr}^{-1}\ \mathrm{eV}^{-1}$. We observe a dip in the energy spectrum near $10^{18.5}$ using the higher resolution stereo data. A 3×10^{20} eV shower was detected by the monocular Fly's Eye on 1991 October 15.

Subject headings: cosmic rays — instrumentation: detectors

1. INTRODUCTION

Every well-determined feature of the cosmic-ray energy spectrum will have considerable impact on theories of the origin, acceleration, and propagation of cosmic rays. Thus the search for new features in the energy spectrum is astrophysically interesting. The shape of the energy spectrum below 10^{17} eV is widely considered to be well established although there is still some disagreement about the details around the knee (Lloyd-Evans 1991). After a 30 year effort by many groups such as Volcano Ranch, Haverah Park, Sugar, Yakutsk, Akeno, and Fly's Eye, the details of the energy spectrum above 10^{17} eV are still limited by statistics, systematics, and resolution. Experimentalists have been searching for the existence of a cutoff on the energy spectrum above 10^{19} eV for more than 25 years. This cutoff could result from the interaction of cosmic-ray protons or nuclei and the 2.7 K black body radiation (Greisen 1966; Zatsepin & Kuzmin 1966; Hill & Schramm 1985; Stecker 1989; Yoshida & Teshima 1990) if the sources are distant enough. The results of these searches are still inconclusive.

Earth's atmosphere makes the low flux of extremely high energy cosmic rays detectable by converting the cosmic-ray primaries into extensive air showers (EASs) of various secondary particles. There are no methods of directly detecting the primaries at these energies; hence, all the information about the primary must come from indirect measurements. Even the indirect measurement is not complete in the sense that only a very small portion of the secondaries is typically sampled by a detector. Considering the difficulties of interpreting these data, it is not hard to understand why there is some degree of disagreement among the existing measurements.

At present two techniques exist for detecting those secondaries—widely spaced ground arrays and the atmospheric fluorescence detector (Fly's Eye). The widely spaced ground array is designed to sample the charged secondary particles. The density of such particles at about 600 m from the core is believed to be proportional to the primary energy and insensitive to the primary composition. The advantages of the ground arrays include an efficient duty cycle, ease of operation, and less sensitivity to atmospheric variations, etc. There are, however, significant difficulties in interpreting ground array data: fluctuations in shower development affect the particle density even far from the core; limited sampling of the shower particles leaves uncertainty in the measured particle density at 600 m; interpretation of the data depends on the interaction model, but no experimental basis for such models is available in this energy range. In spite of these limitations, valuable studies have been performed by the ground array groups in terms of measuring the cosmic-ray flux and reducing the uncertainty of the primary energy. Nevertheless, significant questions still remain about the energy scale and overall systematic effects. The Fly's Eye technique offers a very different approach. The Fly's Eye is designed to collect the atmospheric nitrogen fluorescence light produced by air shower particles. It is the only detector capable of measuring the individual longitudinal shower profile, thus allowing a direct estimation of the primary energy (essentially independent of interaction model). This method is free from problems listed above for the ground arrays, but it faces its own difficulties such as subtraction of the direct and scattered Cerenkov light, the small duty cycle (10% of the total time), and the effect of variable weather conditions. It is also technically more demanding both in operation and data analysis. With the exception of the low duty cycle, most of these problems can be dealt with through careful monitoring and calibration.

In this paper, we present the energy spectrum measured by the Fly's Eye detector operated in monocular mode (since 1981) and in stereo mode (since 1986), together with discussion and comparisons with other experiments. Several interesting

[1] Department of Physics, University of Illinois at Urbana-Champaign, Urbana, IL 61801.
[2] High Energy Astrophysics Institute, Department of Physics, University of Utah, Salt Lake City, UT 84112.
[3] Department of Physics and Mathematical Physics, University of Adelaide, Adelaide, South Australia 5004, Australia.
[4] Present address: Central Oregon Community College, Science Department, Bend OR 97701.
[5] Present address: Department of Physics, The University of Michigan, Ann Arbor, MI 48109.

features of the depth-of-shower maximum (X_{max}) distribution are also presented since they may correlate with structure in the energy spectrum.

2. THE FLY'S EYE EXPERIMENT

The details of the experiment have been described in earlier papers (Baltrusaitis et al. 1985*a*; Cassiday 1985). Only a brief description will be given here. The Fly's Eye detector began full operation in 1981 at Dugway, Utah (40°N, 113°W, atmospheric depth 860 g cm^{-2}). The original detector, Fly's Eye I, consists of 67 spherical mirrors of 1.5 m diameter, each with 12 or 14 photomultipliers at the focus. The mirrors are arranged so that the entire night sky is imaged, with each phototube viewing a hexagonal region of the sky 5°.5 in diameter. In 1986 a second detector (Fly's Eye II) 3.4 km away came into full operation. Fly's Eye II consists of 36 mirrors of the same design. This detector only views the half of the night sky in the direction of Fly's Eye I. Fly's Eye II can operate as a stand-alone device or in conjunction with Fly's Eye I for a stereo view of a subset of the air showers. There are 880 photomultiplier tubes in Fly's Eye I and 464 in Fly's Eye II in total.

2.1. *Detection Mechanism*

Four basic mechanisms contribute to the generation of the light signal seen by the Fly's Eye detector: nitrogen fluorescence, direct Cerenkov light, air molecule (Rayleigh)–scattered Cerenkov light, and aerosol (Mie)–scattered Cerenkov light. Of these, fluorescence relates most directly to the local number of charged particles in an EAS. The intensity of direct and scattered Cerenkov light depends on the history of the charged particles, the incident angle to the atmosphere, and the viewing angle from the detector.

Most of the energy of the primary cosmic ray is dissipated in the atmosphere. Nearly all of the resulting optical fluorescence comes from the $2P$ band system of molecular nitrogen and the $1N$ band system of the N_2^+ molecular ion. Most of the light in the fluorescence spectrum is emitted in the spectral region 310–440 nm. The resultant fluorescent yield integrated over our spectral response is mildly altitude- and temperature-dependent. The light yield corresponds to a scintillation efficiency of only 0.5%. However, the large number of particles in the shower makes the detection feasible for extremely high energy cosmic rays. The fluorescence light is emitted isotropically from the shower, allowing for detection of showers at large distances.

Electrons in an EAS generate Cerenkov light that is primarily beamed in the forward direction. The amount of Cerenkov light at any point along the shower front depends upon the previous history of the shower, and thus it is not proportional to local shower size as is the case for fluorescence light. The Cerenkov beam builds up quickly around shower maximum and remains intense, even after the shower dies away. Direct Cerenkov light dominates the light seen by the Fly's Eye detector at emission angles less than 25°; this makes the inference of size difficult for early stages of shower development which are typically seen at small emission angles. Moreover, as the Cerenkov light builds up with the propagating shower front, the resultant intense beam can generate enough molecular and aerosol scattered light at low altitudes to compete with the locally produced scintillation light. However, the scattered Cerenkov light constitutes in the worst case situations no more than 30% of the total light seen, whereas the directly beamed Cerenkov light at small angles may swamp scintillation light by a factor of 100. These considerations severely limit the accuracy of shower size measurement for those showers striking within 1 km of the detector, and we therefore require events to have R_p (the perpendicular distance from shower track to Fly's Eye) greater than 1.5 km in our analysis.

2.2. *Fly's Eye Detector*

Light collected by the Fly's Eye mirrors is measured by photomultiplier tubes (PMTs) in the focal plane. The PMT signal is split into three trigger channels. Each tube passes the signal through a low-pass Bessel (or RC) filter optimized for nearby (RC constant set at 150 ns since these signal pulse widths are narrow), moderate (700 ns), and distant (1700 ns) showers, respectively. The discriminator threshold for each tube is automatically adjusted to maintain a constant 50 Hz singles rate. This rate is dominated by sky noise. Three corresponding integrating channels with different integration times (3 μs, 8 μs, and 18 μs) exist for the optimization of the signal to noise ratio for different pulse width signals. For a mirror to be triggered, at least two triggering tubes (or for mirrors close to the horizontal, three tubes) within a certain time period (8 μs for the fast channel, 20 μs for the intermediate channel, and 50 μs for the slow channel) are required. The event is recorded when two or more mirrors are triggered within a time window (the time windows are 8 μs, 20 μs, and 40 μs for the fast, medium, and slow channels, respectively). For each triggered event, the tube signals including the trigger time from the fastest channel and the three integrals are saved, together with the threshold of the tube at the time of trigger. The nightly raw data files pass through an automatic filter program and are then manually scanned to remove remaining noise events. Events passing the manual scan are then passed to the analysis procedures described later in this section.

The absolute tube gain and mirror optical efficiency are calibrated once or twice per year. An optical pulser is permanently installed in each mirror housing unit to monitor the relative efficiency of the whole system between calibrations. Twenty-eight vertical flashers are mounted around Fly's Eye I and fire hourly to monitor the atmospheric conditions and to serve as a cross-check for the tube and mirror efficiency. Before each night's run, a comprehensive electronics diagnostic program is run by the operator.

The Fly's Eye detector is the first successful air fluorescence EAS detector. Since it was a developmental project, numerous changes and improvements have been made to the technique during the operating period. The running period is divided into five epochs to account for the changes in hardware and optics. By convention, epoch 1 is from 1983 February to 1985 May. This corresponds to the initial phase of the detector. Optical filters were installed to reduce the sky background at the start of epoch 2 (1985 November to 1987 June). During this period, Fly's Eye II was constructed and went into operation on 1986 November. At the end of epoch 2, anodized mirrors were installed to maintain the reflection efficiency relatively constant over a long time period. The degradation of mirror reflectivity has been only a few percent per year since the coating was applied. At the beginning of epoch 4 (1988 July to 1990 April), the fast channel (for nearby showers) was removed from Fly's Eye I electronics. This was an experiment to determine if decreasing the efficiency for nearby tracks would lower the threshold for distant tracks. Results indicated that we gained

no significant high energy aperture so in epoch 5 (1990 May to 1992 July), the fast channel trigger was reinstalled.

2.3. *Sky Noise*

Noise mechanisms limiting detector sensitivity include star light, zodiacal light, diffuse radiation from the galaxy, light produced by photochemical processes in Earth's ionosphere, and scattered man-made light. This background light induces a DC signal in any phototube aimed at the night sky and fluctuations in this DC signal constitute the sky noise (signals from phototubes are AC-coupled to the electronics).

An analysis of the sky noise in existing Fly's Eye data has been performed. As mentioned in the last section, three integration channels are available for each PMT. Their widths are 3 μs, 8 μs, and 18 μs. For a PMT triggered by a real signal of pulse width less than 8 μs, the difference between the integrals in the 8 μs channel and 18 μs channel is mostly due to sky noise, provided the relative gain and pedestal effects are carefully corrected for. Vertical flasher events are chosen as triggers for the noise analysis as their geometries are well known and tubes with flasher signal pulse widths of less than 8 μs can be selected. The noise (counted in photoelectrons at the phototube cathode) in a 10 μs window is shown in Figure 1. The data can be well described by a Gaussian function with a standard deviation of about 60 photoelectrons. After subtracting the pedestal fluctuations, the residual sky noise σ is 50 photoelectrons per 10 μs, which corresponds to a DC noise of 0.25 photoelectrons per nanosecond per tube at Fly's Eye I. The data show that the sky noise is quite uniform in terms of zenith angle (from 30° to 80°). A slight seasonal effect is seen from the data. The average DC noise is about 0.2 photoelectrons per nanosecond per tube in the summer and autumn and 0.3 photoelectrons per nanosecond per tube in the spring and winter. The night sky brightness from other measurements (Allen 1973) is about 8×10^5 photons m^{-2} μs^{-1} sr^{-1}. This corresponds to 0.36 photoelectrons per nanosecond per tube after considering the Fly's Eye optical reflectivity, tube quantum efficiency, mirror area, tube opening angle, and the optical filter transmittance. The number is in reasonable agreement with our measurement. A correlation study between the tube threshold and the sky noise shows that the Fly's Eye electronics tracks the sky noise variation very well.

2.4. *Data Analysis*

The air shower reconstruction is divided into a series of steps which fall into two major divisions: geometric reconstruction and shower profile reconstruction.

Briefly, the geometric reconstruction begins with determining the shower detector plane from the tube hit pattern. Once this plane is determined, the remaining parameters for an EAS trajectory are the impact parameter R_p and incident angle ψ in the plane. The relationship between these parameters and the tube trigger times can be expressed as (Baltrusaitis et al. 1985a):

$$t_i = t_0 + \frac{R_p}{c} \tan\left(\frac{\theta_i}{2}\right),$$

where c is the speed of light, t_i is the ith tube trigger time, and θ_i is the emission angle from the track to the ith tube; θ_i is related to ψ by

$$\theta_i = \pi - \psi - \chi_i ,$$

where χ_i is the tube elevation angle in the plane. t_0 stands for the time the shower front plane passes through the detector. For short tracks, the above function $t_i(\theta_i)$ is difficult to distinguish from a straight line. In that case, only two of the three parameters can be determined, so R_p and ψ are not independently identified. In order to decouple these two parameters, a long track length in angular space ($\geq 40°$) is necessary. The resolution of both R_p and ψ depends strongly on the track length.

If a shower is seen simultaneously by Fly's Eye I and II, a shower detector plane for each detector can be determined and the intersection of those planes defines the shower trajectory. With this stereo reconstruction, no timing information is needed except to distinguish between upward and downward tracks. However, stereo reconstruction becomes difficult when the opening angle between the planes is too small. This happens when a shower falls in a narrow region along the line between the two detectors or is very distant from Fly's Eye I and II. Except for those small opening angle events, the stereo reconstruction usually yields smaller errors and less pronounced tails in error distribution than the monocular fit.

Once the track geometry is known, the tube signals are sliced into 6° angular bins along the track. The EAS longitudinal size $N_e(x)$ for each angular bin is calculated via an iterative process to remove the contributions due to the direct and scattered Cerenkov beam (Baltrusaitis et al. 1985a). The residual photoelectrons (after the Cerenkov contribution is removed) are due to the atmospheric scintillation process and therefore directly proportional to the charged particle size in the angular bin. Various attenuation effects between source and detector such as ozone absorption, aerosol scattering, and Rayleigh scattering are taken into account (Baltrusaitis et al. 1985a). Finally, each resultant longitudinal profile is fitted with two functions in order to obtain best estimates of (1) the shower size at the maximum development $N_{\max}$, (2) the location of maximum development $X_{\max}$, and (3) the track length integral of the longitudinal profile $\int N_e(x)dx$. The two functions used are (1) an unconstrained (three free parameters) Gaisser-Hillas shower development function of the form (Gaisser & Hillas 1977)

$$N_e(x) = N_{\max}\left(\frac{x - x_0}{X_{\max} - x_0}\right)^{(X_{\max} - x_0)/\lambda} e^{(X_{\max} - x)/\lambda},$$

where x_0 is the depth of first interaction and $\lambda = 70$ g cm^{-2}; and (2) a three-parameter Gaussian function. With the limited resolution of Fly's Eye, the two do almost equally well. Finally, the energy of the primary particle is obtained from either the Gaussian or the Gaisser-Hillas integral:

$$E = \frac{\epsilon_0}{X_0} \int N_e(x)dx ,$$

where ϵ_0/X_0 is the ratio of critical energy of an electron to the radiation length in air and is taken as 2.18 MeV $(\text{g cm}^{-2})^{-1}$ (Dozkhenko & Pomanskii 1964; Rossi 1952; Baltrusaitis et al. 1985b). In addition, we apply an energy-dependent (roughly 10%) correction (Linsley 1983) to account for undetected energy (energy loss through channels which do not contribute to the scintillation light).

2.5. *Aperture Modeling (Monte Carlo)*

A detailed Monte Carlo program for the Fly's Eye detector has been developed to model the energy-dependent detector aperture as well as to test the reconstruction programs. For a given energy, the Monte Carlo program generates a one-dimensional shower profile according to the Gaisser-Hillas parameterization with a mean $X_{\max}$ consistent with the Fly's

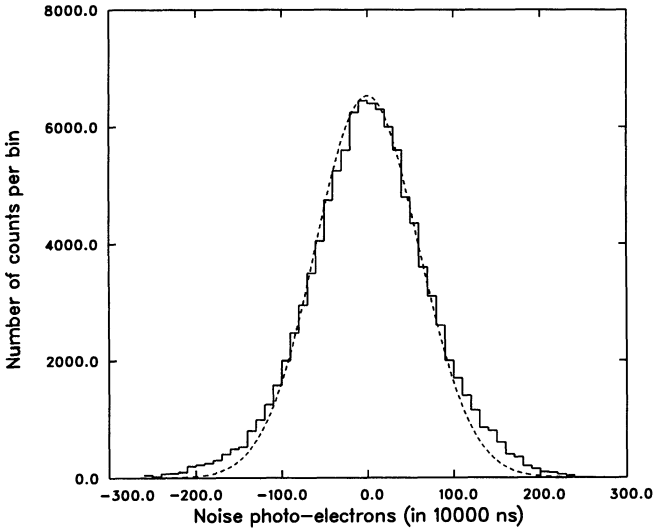

FIG. 1.—Sky background noise in photoelectrons detected by the Fly's Eye tubes in 10 μs time intervals. The curve corresponds to a Gaussian distribution with $\sigma = 60$ photoelectrons.

Eye data. Fluctuations in the depth of first interaction are introduced and the geometry of the track is randomly generated. The resultant photoelectron number at the phototubes due to scintillation and Cerenkov (both direct and scattered) light is calculated including attenuation along the path. In addition to the real signal, the fluctuation of the background sky noise based on our measured numbers is also included as part of the tube signal. Appropriate approximations are used to model the effect of the electronics on the pulse shape. The average thresholds recorded from Fly's Eye running are used to determine if a given tube will trigger. The local (intramirror) and master (intermirror) coincidence requirement is emulated based on the tube trigger pattern and relative trigger times.

This detailed Monte Carlo enables us to model the detector not only in its average behavior but also to some extent to understand the tails of the distributions. This makes our aperture calculation feasible. In a later section, we will show how well we can model the detector trigger aperture.

3. ENERGY RESOLUTION AND SYSTEMATICS

Before presenting results, we first discuss the Fly's Eye energy resolution and systematics. The energy uncertainty comes from the fluorescence efficiency, the atmospheric scattering and transmission of light, Cerenkov subtraction, and uncertainties in track geometry reconstruction. The contributions from each individual source in terms of systematic shift and energy resolution are examined in the following sections.

The air fluorescence efficiency has been measured by a number of groups. It is typically measured either for pure N_2 at low pressures by molecular spectroscopists or in air at pressures that correspond to high-altitude airglow phenomena of interest to atmospheric physicists. Simple kinetic theory arguments relate the fluorescence efficiencies at various pressures. Bunner (1964) has combined all known data up to 1963 and extracted best fits for the fluorescence spectrum of air at tropospheric pressures of interest to this experiment. The estimated uncertainty in the light yield integrated over the wavelength region of 300–400 nm is 20%. More recent experimental work (Hartman 1968; Hughes 1985) has tended to confirm Bunner's numbers, but no recent systematic reevaluation has been done. Hence we use the original uncertainty estimates to set the systematic error on the energy from this source. The uncertainty in the scintillation efficiency in air amounts to a systematic energy error of 20%.

Since the scattered light intensity and the attenuation along the path depend on atmospheric conditions, the atmospheric model is a very important component in our reconstruction programs. The model used has an exponential atmospheric profile with a scale height of 7.5 km. The aerosol profile is also described by an exponential function with a scale height of 1.2 km, and the aerosol concentration corresponds to an aerosol horizontal extinction length of 20 km at ground level. We have compared our model with a widely used and well-verified detailed atmospheric Monte Carlo program (Modtran VII; Kneizys et al. 1988) for calculating light scattering (both Rayleigh and aerosol) and transmission in the air. In Modtran, six geographical-seasonal model atmospheres are provided with 10 choices of aerosol profiles. In our case, the combination of the "1976 US Standard" atmospheric model with the desert aerosol profile for altitudes less than 4 km (in this case, the aerosol scale height below 4 km is 3 km) is most appropriate. Aerosol profiles from our model and the Modtran model intersect around 2–3 km above the Dugway elevation (1.6 km above sea level). The atmospheric ozone content is updated in Modtran using the most recent data. In that program, Rayleigh scattering is calculated by carefully taking account of the wavelength correction of the refractive index in the air as well as the correction due to the optical anisotropy of the air molecules (Shettle, Kneizys, & Gallery 1980; Penndorf 1957). The trigger efficiencies resulting from the use of these two different atmospheric models differ by no more than 10% at all energies measurable by Fly's Eye. To study the relative energy shift induced by these two models, we simulated showers with the above two atmospheric models and reconstructed them with our standard reconstruction programs. At 0.3 EeV, the energy from Modtran is about 3% lower than that from the simple model. At 10 EeV, the former is about 2% higher. The differences are minor both for the trigger aperture and energy calibration. This means the simplified atmospheric model we are using is suitable for our purpose. Figure 2 shows the path length (distance from the tube to the point in shower viewed by that tube) distribution for stereo events above 3×10^{17} eV. The distribution is peaked at 3–4 km, much less than the

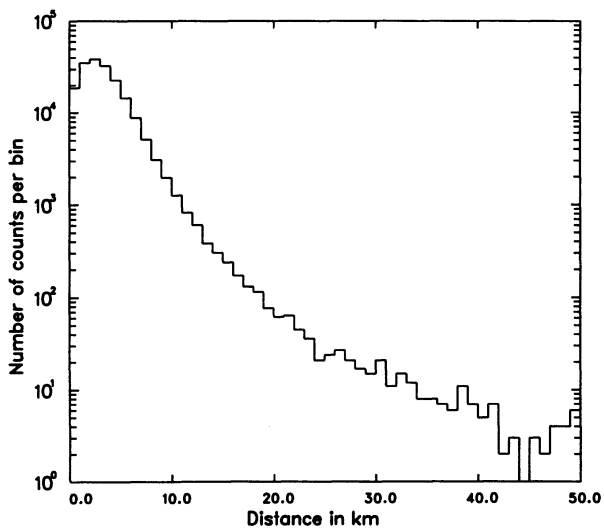

FIG. 2.—Path length distribution between light source and triggered tubes

aerosol extinction length. That explains why the Fly's Eye data are not so sensitive to the aerosol models.

We have also examined the effects of the fluctuations of the atmospheric conditions by varying the aerosol density by 50%. This corresponds to the maximum summer/winter variation in aerosols at Dugway Proving Ground as determined by horizontal visibility variation (Sokolsky 1990; DPG Meterological Group 1992). The variation of the aperture is no more than 10% at all energies. Around 3 EeV, if the real aerosol concentration is 50% less than the model assumption, the energy is overestimated by 6%. The energy is underestimated by 13% if the aerosol density fluctuates 50% more than the model assumption. We thus believe that uncertainties in the atmospheric model and fluctuations about the average atmosphere induces a maximum systematic uncertainty of 10% on both aperture and the reconstructed energy since the mean fluctuation in the aerosol density is smaller than the extremes considered above.

Another parameter which affects the energy estimation is the angular distribution of the Cerenkov beam. This affects the part of our shower data detected at very small viewing angles. The Cerenkov photons emitted by the charged shower particles in the air essentially maintain the same direction as the charged particles; thus, the angular distribution of shower Cerenkov light is determined by the angular distribution of charged particles. Studies of multiple scattering show that the angular distribution of ionizing particles averaged over the length of the EAS can be represented by

$$\frac{dN}{d\Omega} \propto \frac{1}{2\pi\theta_0 \sin\theta} e^{-\theta/\theta_0},$$

where $\theta_0 = aE_T^{-b}$, E_T being the threshold energy for Cerenkov emission $\{E_T[\mathrm{MeV}] = 0.511[2(n-1)]^{-1/2}\}$ for electrons. n is the refractive index. There have been three calculations of parameters a and b, and they result in (0.83, 0.67) (Stanev et al. 1981), (0.77, 0.65) (Elbert, Stanev, & Torii 1983), and (0.85, 0.66) (Hillas 1982), respectively. We have measured θ_0 directly using stereo data (Baltrusaitis et al. 1987) and find $\theta_0 = 4.^{\circ}0 \pm 1.^{\circ}2$, in agreement with the above calculations. The parameters from Stanev et al. are the ones currently used by Fly's Eye Monte Carlo and reconstruction programs. We have simulated showers with the above three parameterizations and reconstructed them with the first pair. The reconstructed energy from the first combination is slightly higher than the other two, but the maximum difference is less than 4%. We therefore assign a systematic uncertainty of 4% from this source to the energy determination.

The detector Monte Carlo was written based on our understanding of the detector performance. A self-consistency check has been performed with the Monte Carlo and the reconstruction programs. For the monocular case, if the track geometry is calculated perfectly, the reconstructed energy is less than the input energy by 6%. This is due entirely to the Gaussian approximation of the shower profile. We correct our energy by this factor.

Systematic shifts in geometrical reconstruction can induce shifts in energy. We check this effect by Monte Carlo. In the stereo case, there is no systematic shift between the input and the reconstructed R_p. However, the monocular reconstruction program tends to underestimate R_p and therefore to overestimate the zenith angle of the track. Reconstruction using monocular data thus systematically introduces a 20% energy shift. A similar shift is seen for real events when comparing energies analyzed using monocular reconstruction and the more reliable stereo reconstruction. This systematic shift in energy is corrected for in our data analysis. For the stereo case, the geometrical reconstruction error is much smaller, resulting in a total energy shift of 10%. The residual contribution to the systematic error from this geometric correction is estimated to be less than 5%.

The best way to study the energy resolution is to compare the energy calculated independently by Fly's Eye I and Fly's Eye II for events registered by both eyes. Here stereo reconstruction is used so that the contribution from the geometrical reconstruction error is small (Monte Carlo shows that the R_p resolution of stereo reconstruction is typically at 5%–6%; therefore its contribution is really negligible). Figure 3 shows histograms of the fractional energy discrepancy between FE I and FE II, $(E_1 - E_2)/E_{\mathrm{average}}$, for two energy ranges. Here E_1 is the energy as measured from Fly's Eye I information only and E_2 from Fly's Eye II. The systematic shift between Fly's Eye I and II is about 2.5%. This number shows that we have very good relative energy calibration control over the entire running period. The distribution has a standard deviation of 0.47 for events below 2×10^{18} eV and 0.40 for events above; hence, the single-eye energy resolutions (using stereo reconstruction) are 33% and 28% for these energy ranges. The resulting stereo energy resolutions are 24% and 20%, respectively (another factor of square root of 2 down because of 2 times more tubes per track). Similarly we get the monocular energy resolution (for the sample of events also seen in stereo) by comparing the monocular energy with the stereo energy on an event by event basis. Figure 4 also shows the histograms of $\log(E_{\mathrm{mono}}/E_{\mathrm{stereo}})$ for two energy ranges. From Figure 4 we see that the peak is right at 0 which means we have very good energy cross-calibration between stereo and monocular reconstructed events once the offset caused by systematic geometrical error of monocular reconstruction has been corrected for.

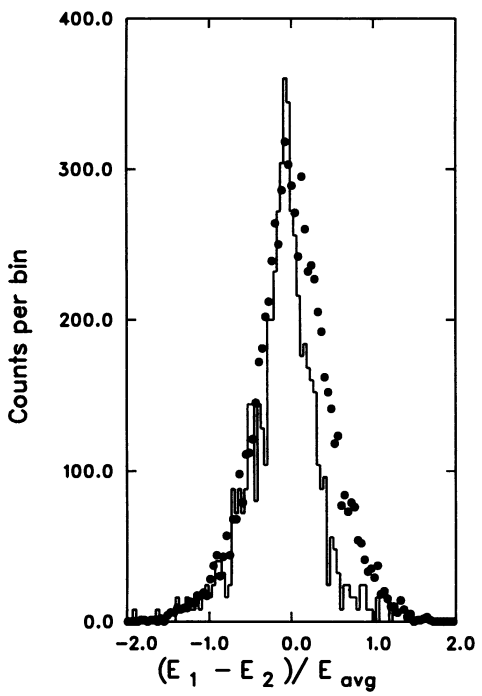

FIG. 3.—Relative fluctuations between energy reconstructed by FE I and FE II. *Dots*: events below 2×10^{18} eV. *Solid line*: events above 2×10^{18} eV (the counts are scaled by a factor of 8 for comparison).

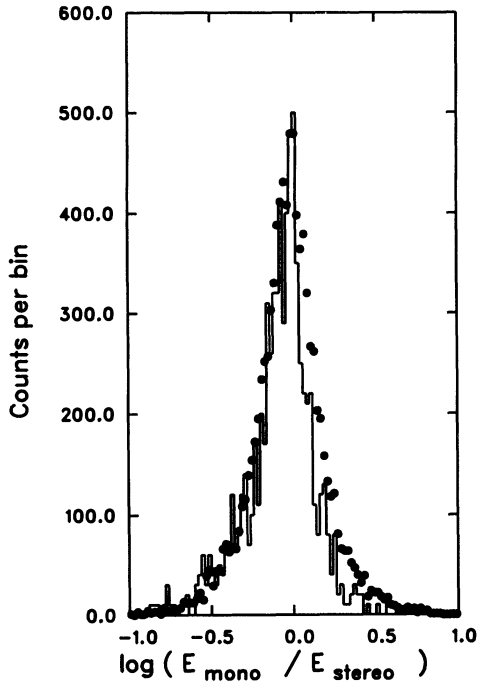

FIG. 4.—Relative fluctuations between energy reconstructed by monocular eye and stereo eyes. *Dots*: events below 2×10^{18} eV. *Solid line*: events above 2×10^{18} eV (the counts are scaled by a factor of 10 for comparison).

The full width at half-maximum of the log ($E_{\rm mono}/E_{\rm stereo}$) distribution is 0.348 for events below 2 EeV and 0.284 for events above 2 EeV. After subtracting the stereo energy resolution, the resulting monocular energy resolutions are 36% for events below 2 EeV and 27% for events above 2 EeV. It should be pointed out that the monocular resolutions are underestimated a little bit because stereo energy is not completely independent of monocular energy.

In conclusion, we estimate our systematic uncertainty (including the uncertainty of the air scintillation efficiency) for the energy determination to be no more than 40% (in the unlikely situation that all the systematics shift the energy in the same direction). The stereo data have better energy resolution (20%–24%) than the monocular data (27%–36%) mainly because of the improvement in the geometrical reconstruction.

4. RESULTS

The results presented below consist of two parts. In the first part, we discuss the structure of the spectrum using our well-measured stereo data; in the second part, we discuss the high-energy tail of the spectrum. Here we use monocular data to increase our statistics as much as possible.

4.1. *The Structure of the Spectrum*

The cosmic-ray spectrum is often thought of as largely featureless. This might be due to the limited energy resolution of previous detectors. We have worked on improving our energy resolution to avoid this problem. The stereo Fly's Eye data have been chosen for this purpose. By requiring that both eyes observe the same events, the stereo aperture is essentially the overlap of the apertures of the two individual eyes; hence, the number of events is reduced compared to the monocular data but the energy resolution is significantly improved. For the data presented below, a very loose cut of 100% estimated fractional energy uncertainty has been imposed. As discussed above, the estimated mean energy resolution is 20%–24%, much smaller than the cut. Table 1 shows the event distribution and the total exposure for the whole running period. Figure 5 shows the energy spectrum derived from the numbers in Table 1. The spectrum becomes steeper right after $10^{17.6}$ eV and flattens after $10^{18.5}$ eV. The change in the spectral slope forms a dip centered at $10^{18.5}$ eV. We divide our stereo energy spectrum into three energy ranges determined by eye and fit them to a power law spectrum in each region. Table 2 shows the normalization and the slope within each region. Also listed in Table 2 is the overall fit regardless of the details of the spectrum, though the overall spectrum does not resemble a single power law. In this paper, all the fits were done with the weighted least-squares method. A comparison has also been done between the weighted least-squares method and the maximum likelihood method. Generally speaking, the two methods show minor differences. For example, an overall stereo spectrum fitting with weighted least-squares method gives spectral slope -3.177 ± 0.013, while the maximum likelihood gives -3.183. The two numbers agree within the error. The overall fit is dominated by the low-energy points, with minor contributions from the points above 10^{19} eV. To show the significance of the dip, the numbers of events expected from the overall fit (renormalized to the observed number of events at $10^{17.6}$ eV) are listed in Table 3 with the observed numbers of events. The expected number of events between $10^{17.6}$ eV and $10^{19.6}$ eV is 5936.3, and the observed is 5477. The significance of this deficit is 5.96 σ. To show the significance of flattening above $10^{18.5}$ eV, we use the normalization and slope from a total fit up to $10^{18.5}$ eV. The total number of observed events above this energy is 281, while the expected number would be 230, which is a 3.4 σ excess. The excess is even more pronounced (5.2 σ) if the spectrum from $10^{17.6}$ to $10^{18.5}$ eV is used to calculate the expectation (in this case, the expectation is 205.9 events above $10^{18.5}$ eV). From Figure 3 we see that the energy resolution over this region is approximately constant; hence, the spectral break is not produced by resolution effects.

To show that the dip is not an artificial result of the aperture calculation, we have plotted our event energy distribution weighted by $E^{1.5}$ in Figure 6. A dip is clearly present in the raw data itself.

4.2. *The Spectrum near the Greisen-Zatsepin-Kuzmin Cutoff*

In this section our emphasis will be on the high end of the energy spectrum. Compared to the stereo data set which we have already discussed, the monocular data set is much bigger but has to rely on the tube trigger times for reconstruction. The

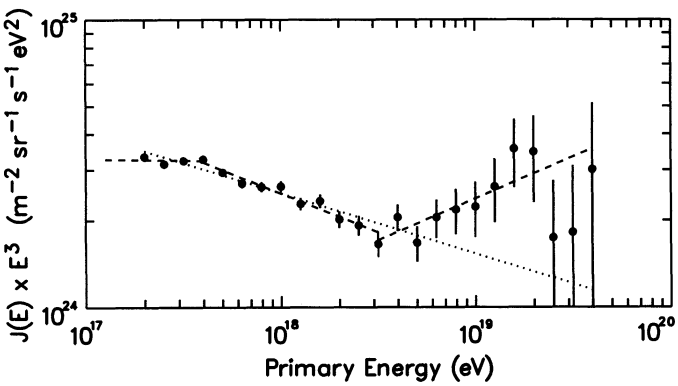

FIG. 5.—Fly's Eye stereo energy spectrum. *Points*: data. *Dashed line*: best fit in each region. *Dotted line*: best fit up to $10^{18.5}$ eV.

TABLE 1

LIST OF NUMBER OF EVENTS, EXPOSURE, AND FLUX

Energy Bin $\{\log_{10}[E(\text{eV})]\}$	Number of Events	Exposure (hr km^2 sr)	$\log_{10}$ (flux) (s^{-1} eV^{-1} m^{-2} sr^{-1})	$\log_{10}(JE^3)$ (s^{-1} eV^2 m^{-2} sr^{-1})
17.3	883	12699	−27.377	24.523
17.4	980	23691	−27.703	24.497
17.5	1052	39260	−27.991	24.509
17.6	1050	61404	−28.286	24.514
17.7	902	92780	−28.632	24.468
17.8	761	135380	−28.970	24.430
17.9	658	191006	−29.282	24.418
18.0	571	261450	−29.580	24.420
18.1	416	347227	−29.941	24.359
18.2	344	444622	−30.231	24.369
18.3	229	544500	−30.596	24.304
18.4	162	640088	−30.916	24.284
18.5	101	733782	−31.281	24.219
18.6	89	827875	−31.488	24.312
18.7	51	920678	−31.876	24.224
18.8	43	1006744	−32.089	24.311
18.9	31	1079666	−32.361	24.339
19.0	21	1132708	−32.651	24.349
19.1	16	1163796	−32.881	24.419
19.2	14	1192204	−33.050	24.550
19.3	9	1243732	−33.360	24.540
19.4	3	1308175	−33.959	24.241
19.5	2	1325003	−34.241	24.259
19.6	2	1267240	−34.321	24.479

time fitting tends to yield larger geometrical errors and therefore larger uncertainty in the energy determination. We make loose geometrical resolution cuts on the monocular data and no cut on the energy resolution, so as to keep the statistics as large as possible and avoid possible high-energy event losses.

TABLE 2

NORMALIZATIONS AND SPECTRAL SLOPES OF $J(E)$

Energy Range (eV)	Power Index	log (normalization)	Normalized at
$10^{17.3}$–$10^{19.6}$	-3.18 ± 0.01	−29.593	10^{18} eV
$10^{17.3}$–$10^{17.6}$	-3.01 ± 0.06	−29.495	10^{18} eV
$10^{17.6}$–$10^{18.5}$	-3.27 ± 0.02	−29.605	10^{18} eV
$10^{18.5}$–$10^{19.6}$	-2.71 ± 0.10	−32.623	10^{19} eV

TABLE 3

NUMBER OF EVENTS EXPECTED AND OBSERVED

Energy Bin $\{\log_{10}[E(\text{eV})]\}$	Number of Events Expected from Overall Fit	Number of Events Observed	Excess in σ from Overall Fit
17.6	1050.00	1050	0.00
17.7	961.03	902	−1.90
17.8	849.45	761	−3.03
17.9	725.98	658	−2.52
18.0	601.95	571	−1.26
18.1	484.27	416	−3.10
18.2	375.63	344	−1.63
18.3	278.65	229	−2.97
18.4	198.43	162	−2.59
18.5	137.79	101	−3.13
18.6	94.17	89	−0.53
18.7	63.44	51	−1.56
18.8	42.02	43	0.15
18.9	27.30	31	0.71
19.0	17.35	21	0.88
≥19.1	28.35	46	3.31

Figure 7 shows the event distribution as a function of energy. Figure 8 shows the total exposure using the running time and the simulated aperture for each epoch. We can check how well the Monte Carlo simulates the different running conditions by comparing the calculated apertures and event rates for different epochs. For example, we can compare epoch 3 and 4 apertures and spectra individually. As stated before, the epoch 4 electronics behaves very differently from epoch 3 since the fast channel triggers were turned off. Figure 9 shows the apertures simulated for epoch 3 and epoch 4. From that figure, we can see that epoch 4 has a much smaller trigger efficiency at lower

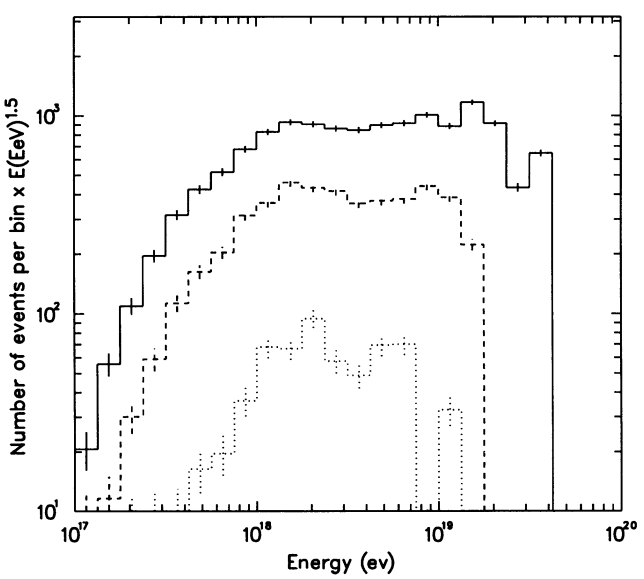

FIG. 6.—Stereo event distribution weighted by $E^{1.5}$ as function of energy resolution cut. *Solid line*: 100% energy resolution cut. *Dashed line*: 10% energy resolution cut. *Dotted line*: 5% energy resolution cut.

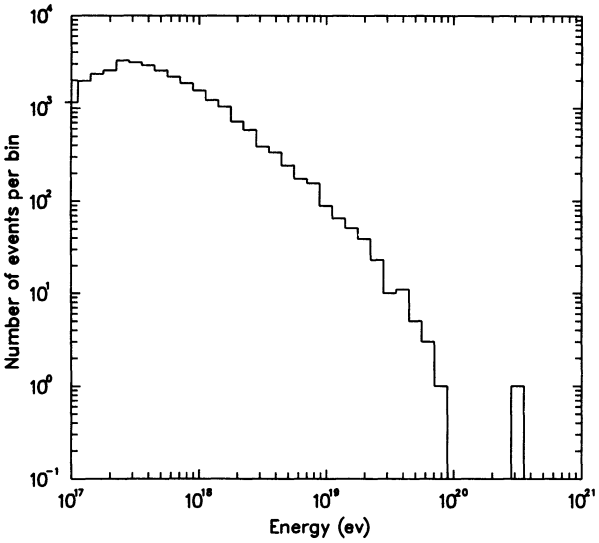

FIG. 7.—The Fly's Eye I monocular reconstruction event distribution as a function of primary energy.

energy. Figure 10 shows the spectra for the above two epochs. The two spectra look almost the same even though the event distribution and the aperture are very different. Similar consistency is found in comparing other epochs. We thus believe that the aperture modeling is sufficiently accurate to describe the various epochs well. The total energy spectrum is shown in Figure 11. Because of the limited energy resolution, the differential energy spectrum observed by the monocular eye (multiplied by E^3) does not show the degree of structure found in the stereo data. The best-fit energy spectrum is $J(E) = 10^{-29.55} \times (E/10^{18}\ \mathrm{eV})^{-3.07\pm0.01}\ \mathrm{m^{-2}\ s^{-1}\ sr^{-1}\ eV^{-1}}$.

Figure 11 shows a flattening of the spectrum above 10^{19} eV. To investigate the significance of the flattening, we have calculated the expected number of events by the slope and normalization determined by data points below 10^{19} eV. Between $10^{19.0}$ eV and $10^{19.9}$ eV, 242.35 events are expected. With 297 events detected, the Fly's Eye observes a 3.5 σ excess above 10^{19} eV. Since the chance probability for such an excess is about 2×10^{-4}, the monocular data support the stereo result that the spectrum flattens after 5×10^{18} eV.

Figure 11 also indicates that the flattening of the spectrum extends for only about one decade and steepens quickly right after $10^{19.7}$ eV. The expected number of events above $10^{19.7}$ eV based on the spectrum between $10^{19.0}$ and $10^{19.7}$ eV $\{J[E] = 10^{22.40} \times [E(\mathrm{eV})]^{-2.89\pm0.15}\ \mathrm{m^{-2}\ s^{-1}\ sr^{-1}\ eV^{-1}}\}$ is

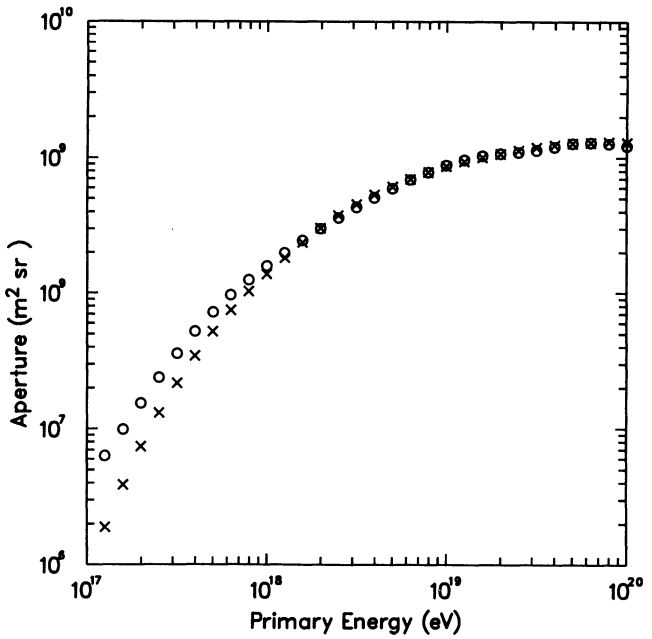

FIG. 9.—Monocular Fly's Eye aperture for epoch 3 and epoch 4. *Circles*: epoch 3; *crosses*: epoch 4.

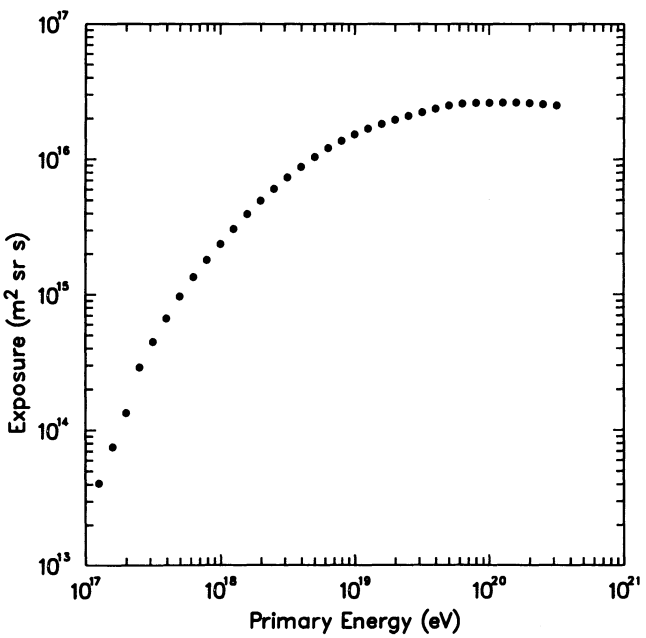

FIG. 8.—Total exposure for the monocular Fly's Eye

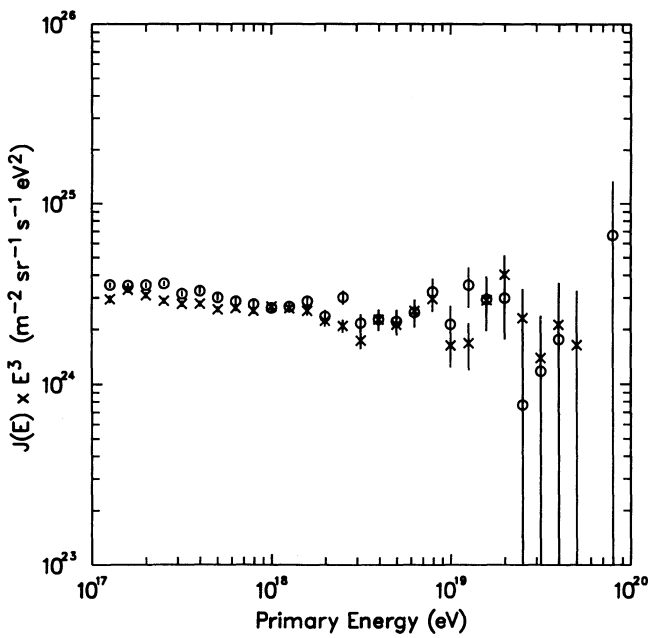

FIG. 10.—Monocular Fly's Eye spectrum for epoch 3 and epoch 4. *Circles*: epoch 3; *crosses*: epoch 4.

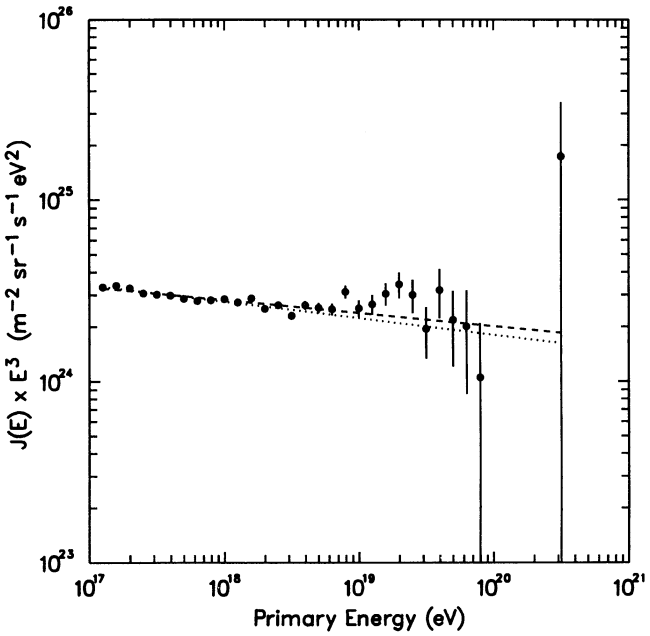

FIG. 11.—Fly's Eye monocular energy spectrum. *Points*: data. *Dashed line*: best fit of the total spectrum. *Dotted line*: best fit up to $10^{18.5}$ eV.

20.63, but we actually only observe 10 events. To confirm this picture, more statistics are needed.

On 1991 October 15, we observed an event at $(3^{+0.36}_{-0.54}) \times 10^{20}$ eV. The event was well measured. The shower profile of this event is consistent with expectations for a normal proton induced shower (Fig. 12). The $X_{\max}$ of this event is 852^{+68}_{-100} g cm^{-2}; the expectation for an average proton event from the proton elongation rate gives 850 g cm^{-2} (Gaisser et al 1993). However, we cannot rule out that it is a gamma-ray–induced shower. The hypothetical gamma-ray spectrum continuing beyond the GZK cutoff has been discussed by a number of authors (Aharonian & Vardanian 1987). With more than a half-decade energy gap between this and the second highest energy event, the nature of the end of the cosmic-ray spectrum appears even more puzzling. A new generation of detectors with much larger apertures is definitely necessary to settle this issue.

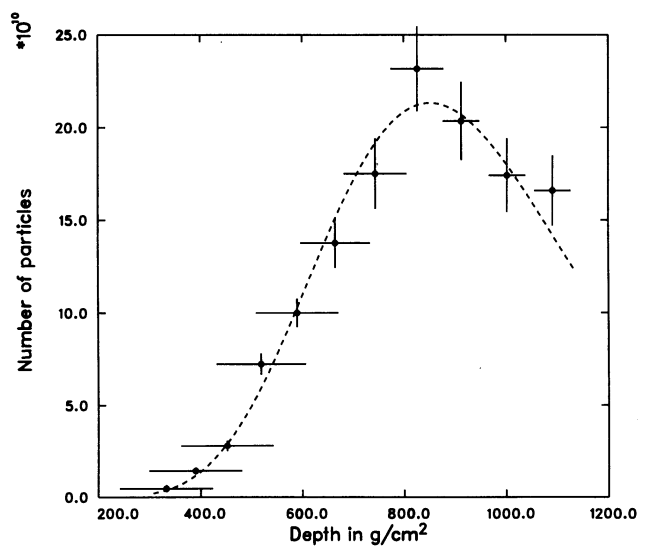

FIG. 12.—Shower profile for the most energetic event observed by the Fly's Eye detector.

5. DISCUSSION

5.1. *Consistency of the Stereo and Monocular Spectrum*

In the last section, we saw that the monocular spectrum is flat and relatively structureless compared to the stereo spectrum. Can the difference be explained by the resolution difference in energy? We performed a Monte Carlo study using the stereo spectrum and the monocular exposure as input, fluctuating the energy according to our monocular energy resolution. This somewhat overestimates the resolution effect since the stereo spectrum is already smeared by the stereo resolution. The resulting simulated spectrum is shown in Figure 13. It almost completely reproduces our monocular spectrum before 3×10^{19} eV. Hence, the gross differences between monocular and stereo spectra can indeed be simply accounted for by the difference in energy resolution.

We have searched for evidence for the dip structure in the monocular data by applying very tight resolution cuts. Since the shape of the aperture varies from epoch to epoch in the monocular data and subtle energy scale shifts can also wash out the dip, we examine the energy distribution separately for each epoch. We expect epochs 3, 4, 5, and 6 to have the best energy resolution since these have the benefit of the best mirror reflectivity and stable calibration. Figure 14 shows the energy distribution for epochs 4 and 5 for events with a projected track length of 60° or greater and an estimated energy resolution of less than 25%. A dip is clearly seen at the same energy as in the stereo data.

5.2. *The Spectrum Slope*

In this section, we discuss the spectrum slope fitted over a wide energy range regardless of the details of the spectrum, or

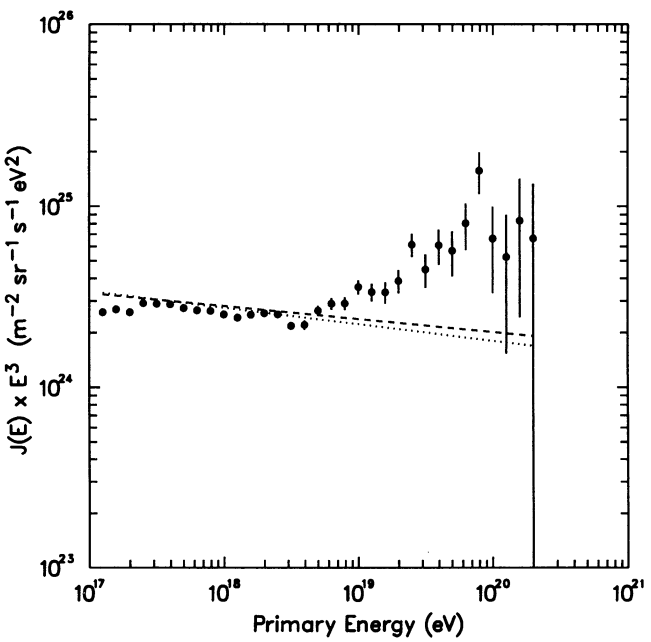

FIG. 13.—Monte Carlo simulated monocular spectrum based on the stereo spectrum and monocular exposure and energy resolution. The dotted and dashed lines are the same as Fig. 11.

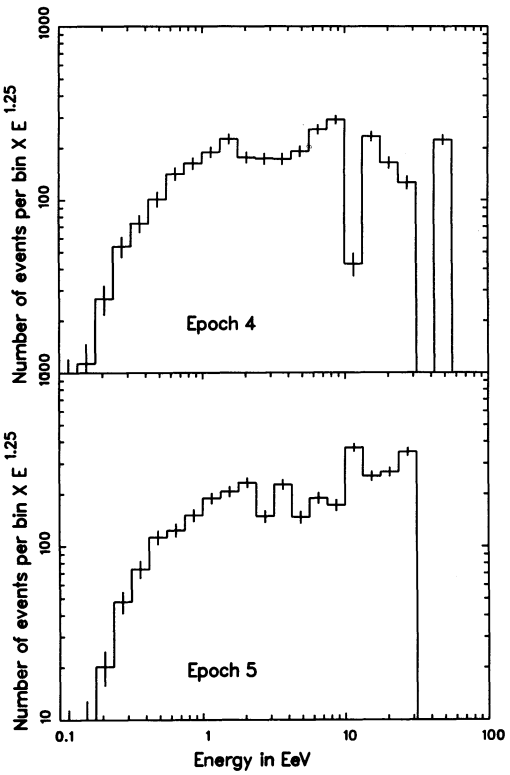

FIG. 14.—The energy distribution for epochs 4 and 5 for events with a projected track length of 60° or greater and an estimated energy resolution of less than 25%.

the so-called overall spectrum slope above 10^{17} eV. Besides the Fly's Eye spectra, the results from Akeno (Nagano et al. 1992), Haverah Park (Watson 1991; Lawrence, Reid, & Watson 1990) and Yakutsk (Efimov et al. 1991; some numbers for Yakutsk are also quoted from Nagano et al. 1992) are also discussed and compared. Figure 15 shows the spectra from Akeno, Haverah Park, and Yakutsk. The three giant air shower arrays listed above are all composed of more than two types of detectors or subarrays with different energy thresholds. For such a combination, it is a good idea to fit the spectrum slope from the various subarrays separately as done by Akeno rather than mixing the data points. Table 4 lists the spectrum slopes fitted by various groups.

If every number in Table 4 is treated equally, the average slope above 10^{17} eV is 3.15. As we already stated, the Fly's Eye stereo data have much better resolution than the monocular data. For the Akeno experiment, Array 1 (detector spacing of 120 m) also has better resolution than Array 20 (detector spacing about 1 km). Comparing the numbers for Akeno Array 1 and Array 20, as well as Fly's Eye monocular and stereo data, it is clear that the poorer resolution experiments tend to underestimate the spectrum slope. Besides the resolution effect, there are also some systematic difference between the experiments, which might be due to the acceptance estimation, energy scale shifts, etc. From Table 4, we find the systematic offset in the spectral slope is less than 0.2.

5.3. *The Dip in the Spectrum*

A dip around $10^{18.5}$ eV is clearly seen from the Fly's Eye stereo spectrum. In Table 5, we list the slopes over a relatively short energy range given by different experiments. There is

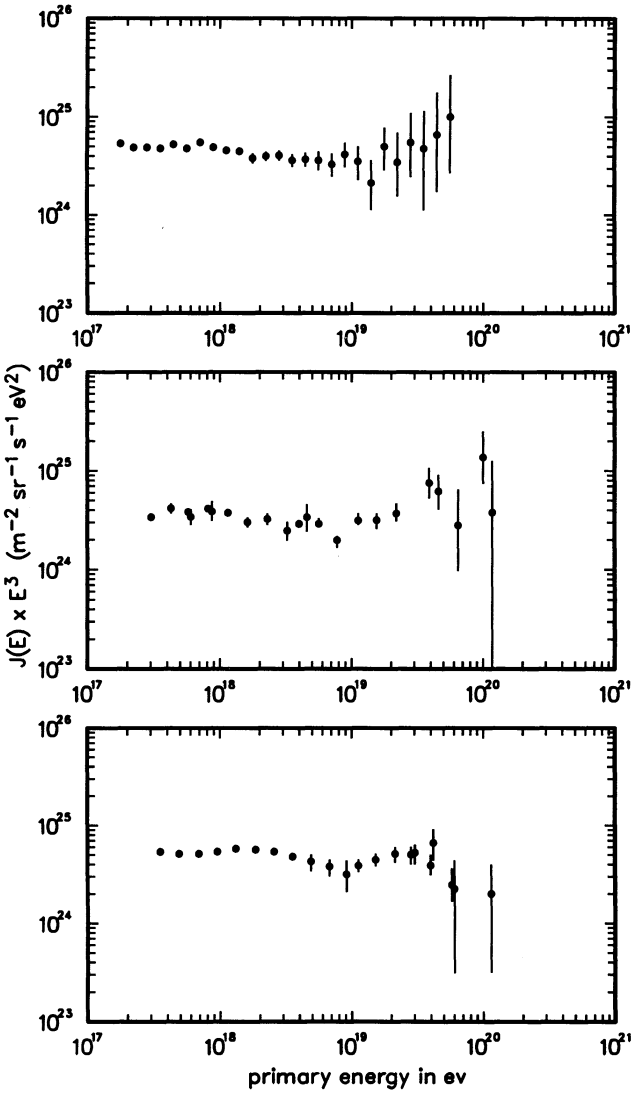

FIG. 15.—Energy spectra for (*top*) Akeno, (*middle*) Haverah Park, and (*bottom*) Yakutsk.

qualitative agreement. The breaks are defined by each experiment independently. Though the Yakutsk result is not listed in Table 5, its spectrum also clearly shows a dip around $10^{18.9}$ eV. Some unique features are listed below. The power index of the spectrum below $10^{17.7}$ eV is close to 3.01. Around $10^{17.7}$ eV, the spectrum power index increases approximately by 0.2, and the spectrum steepening lasts about one decade. Near $10^{18.5}$

TABLE 4

SPECTRUM SLOPES

Experiment	Slope	Energy Range (eV)
Haverah Park	$3.14^{+0.05}_{-0.06}$	$10^{17.6}$–$10^{20.0}$
Akeno	3.04 ± 0.04	$10^{15.7}$–$10^{19.8}$
Akeno (Array 1)	3.24 ± 0.18	$10^{17.8}$–$10^{18.8}$
Akeno (Array 20)	3.16 ± 0.08	$10^{17.8}$–$10^{18.8}$
Yakutsk	3.23 ± 0.08	$10^{18.3}$–$10^{19.0}$
Fly's Eye (mono)	3.07 ± 0.01	$10^{17.3}$–$10^{19.9}$
Fly's Eye (stereo)	3.18 ± 0.02	$10^{17.3}$–$10^{19.6}$

TABLE 5

THE DIP

Experiment	Slope before the Dip	First Slope in the Dip	Second Slope in the Dip
Akeno	3.02 ± 0.03 ($10^{15.7}$–$10^{17.8}$)	3.16 ± 0.08 ($10^{17.8}$–$10^{18.8}$)	2.8 ± 0.3 ($10^{18.8}$–$10^{19.8}$)
Haverah Park	3.01 ± 0.02 ($10^{17.48}$–$10^{17.6}$)	3.24 ± 0.07 ($10^{17.6}$–$10^{18.6}$)	$2.70^{+0.18}_{-0.17}$ ($>10^{19}$)
Fly's Eye (stereo)	3.01 ± 0.06 ($10^{17.3}$–$10^{17.6}$)	3.27 ± 0.02 ($10^{17.6}$–$10^{18.5}$)	2.71 ± 0.10 ($10^{18.5}$–$10^{19.6}$)

eV, the spectrum flattens again. The change in the power index may be as small as 0.36 as estimated by Akeno, or as large as 0.56 as estimated by Fly's Eye. Statistics are not large enough at present for a precise determination of these changes.

It should be pointed out that every group has observed a significant deficit between 10^{18} eV and 10^{19} eV (Nagano et al. 1992; Watson 1991) when compared to expectations of a continuation of the lower energy spectrum. The energy resolution markedly affects the significance of the dip, as demonstrated by the Fly's Eye monocular and stereo spectrum.

5.4. *The Flattening above* 10^{19} eV

From Table 5, almost all the experiments observed a flattening of the spectrum above 10^{19} eV. To what extent do we believe this flattening? Certainly the significance depends on the assumptions of the slope below it. Here we will only examine one hypothesis—suppose the the spectrum power index above 10^{19} eV is the same as the index below this energy. Table 6 lists the number of events expected based on this hypothesis as well as the number of events observed.

If one admits the existence of the dip, one also admits the flattening of the spectrum at the same time (that is how the dip is formed). But the existence of the dip is not a necessary condition for the flattening. The monocular Fly's Eye data shows a 3.5 σ excess even over a flat spectrum extrapolated from below 10^{19} eV.

5.5. *The Cutoff*

The question of the existence of the Greisen-Zatsepin-Kuzmin cutoff is very difficult at present. Table 7 lists the number of events above 10^{20} eV observed by various experiments together with their total exposures (Sokolsky, Sommers, & Dawson 1992). The expected number of events are calculated based on the spectrum above 10^{19} eV from each individual experiment.

Even without counting the further flattening of the spectrum above 10^{19} eV, the monocular Fly's Eye is expected to observe three events above $10^{19.95}$ eV.

5.6. *Possible Hint as to the Cosmic-Ray Origins*

What does the structure of the spectrum tell us? One possibility is that the cosmic-ray origin changes with energy. The break between 2 and 5 EeV may indicate the dominance of a new cosmic-ray source. Before the break, the cosmic rays may be mostly of Galactic origin. After the break, an extragalactic component may be taking over. Due to the Galactic confinement requirement (leakage of the light particles), the Galactic component before the break may have a heavy composition. The Fly's Eye X_{max} distribution shows the cosmic-ray composition is getting lighter over the dip region (for more detailed information about X_{max}, see Gaisser et al. 1993; Bird et al. 1993a); therefore, the emergent component is probably purely protonic. We perform the following test on the above hypothesis. We first fit the Galactic flux and extragalactic flux by assuming that each follows a power law and that the measured spectrum above and below the dip corresponds to the superposition of these two power laws. The best fit results from $10^{17.6}$–$10^{19.6}$ eV are

$$\log [J(E)(m^{-2}\ s^{-1}\ sr^{-1}\ eV^{-1})] = 33.185 - 3.496 \times \log (E)\ ,$$

for the Galactic component, and

$$\log [J(E)(m^{-2}\ s^{-1}\ sr^{-1}\ eV^{-1})] = 16.782 - 2.610 \times \log (E)\ ,$$

for the extragalactic component. The ratio of the Galactic component (iron) to the extragalactic component (protons) as a function of energy can then be expressed as

$$\frac{\text{iron flux}}{\text{proton flux}} = 10^{-0.887 \times [\log (E) - 18.50]}\ .$$

From our earlier composition paper (Gaisser et al. 1993) we see that any reasonable interaction model predicts the difference in mean X_{max} of iron and protons to be about 75 g cm^{-2}, and the elongation rate of a pure composition to be about 50 g cm^{-2}. The expected mean X_{max} based on the KNP hadronic interaction model (Kopeliovich, Nikolaev, & Potashnikova 1989) for the proton/iron mixture given by the expression above is plotted in Figure 16 together with the Fly's Eye data. It can be seen that the simple model described above gives a good approximation of the X_{max} dependence on the energy as well as the (independent) detailed shape of the primary energy spectrum. Such a mixture gives an elongation rate of 81 g cm^{-2} between 10^{18} and 10^{19} eV, very near our observed elongation rate of 78.9 ± 3 g cm^{-2} (Bird et al. 1993a). This picture is also consistent with the absence of statistically significant anisotropy deduced from the Fly's Eye data (Bird et al. 1993b, c). The low-rigidity heavy nuclei below the transition can be isotropized by the Galactic magnetic field. The high-rigidity

TABLE 6

FLATTENING OF THE SPECTRUM

Experiment	Number of Events Expected	Number of Events Observed	Significance
Haverah Park	65.5	106	5 σ
Akeno	32.7	45	2.2 σ
Fly's Eye (mono)	242.35	297	3.5 σ

TABLE 7

NUMBER OF EVENTS ABOVE 10^{20} eV

Experiment	Number of Events Observed	Number of Events Expected	Exposure Exposure (m^2 s sr)
Akeno	0	0.6	3.2×10^{15}
Haverah Park	4	3.2	8×10^{15}
Fly's Eye (mono)	1	5.4	26×10^{15}
Yakutsk	1	14.4	28×10^{15}

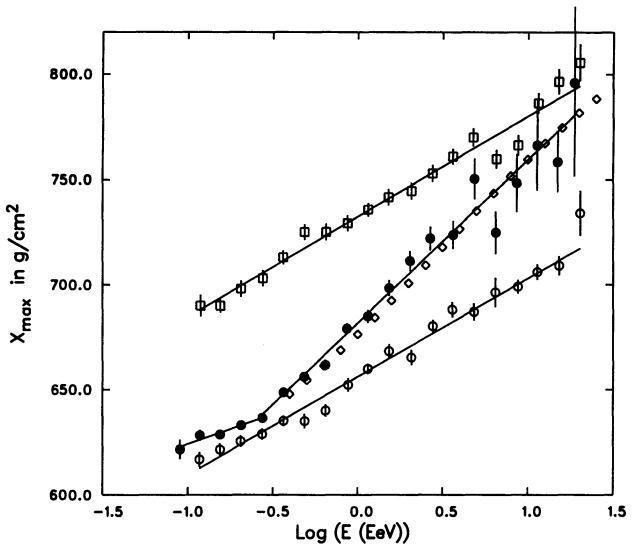

FIG. 16.—X_{max} elongation rate. *Filled circles*: Fly's Eye data. *Open squares*: proton X_{max} distribution based on KNP model. *Open circles*: iron X_{max} distribution based on KNP model. *Diamonds*: expected mean X_{max} distribution based on a simple two-component assumption of cosmic rays.

protons above the transition may represent an isotropic extragalactic cosmic-ray population.

We found that both Figures 5 and 16 show a break near $10^{17.5}$ eV. Though at present we cannot rule out the possibility of a detector threshold effect, this break could be a feature which relates to the propagation or acceleration of cosmic rays. Figure 16 shows that the measured elongation rate is high enough to account for a transition from a heavy composition to a light composition. The pure-iron limit dictates that the elongation rate must have a smaller value at lower energies. The break at $E = 10^{17.5}$ eV satisfies that constraint and may mark the energy of maximum heaviness for the cosmic ray composition.

6. CONCLUSIONS

1. The monocular Fly's Eye has observed a cosmic-ray spectrum with an overall fit

$$J(E) = 10^{-29.55} \times (E/10^{18}\ \text{eV})^{-3.07\pm0.01}\ \text{m}^{-2}\ \text{s}^{-1}\ \text{sr}^{-1}\ \text{eV}^{-1},$$

in the energy range $10^{17.3}$–$10^{19.9}$ eV.

2. With much better energy resolution, the stereo Fly's Eye has clearly observed a dip in the spectrum between $10^{17.6}$ and $10^{19.6}$ eV. This spectral change corresponds to a change in the cosmic-ray composition from predominantly heavy to predominantly light as determined by the Fly's Eye X_{max} measurements.

3. Both monocular and stereo Fly's Eye data indicate a flattening of the spectrum above 10^{19} eV.

4. No definite conclusion can be drawn about the existence of the Greisen-Zatsepin cutoff at this stage. More statistics are required to solve the puzzle.

We would like to acknowledge the earlier contributions of R. M. Baltrusaitis, H. Bergeson, R. Cady, R. Cooper, B. Fick, P. R. Gerhardy, D. Liebing, Y. Mizumoto, and D. Steck to this experiment. In particular, we would like to thank G. Cassiday for his innumerable contributions to the development of the air fluorescence technique. We are indebted to Colonels Frank Cox and James King and the staff of the Dugway Proving Grounds for their continued cooperation and assistance. This work has been supported in part by the National Science Foundation (grants PHY 91-00221 at Utah) and the US Department of Energy (grant FG02-91ER40677 at Illinois).

REFERENCES

Aharonian, F. A., & Vardanian, V. V. 1987, unpublished
Allen, C. W. 1973, Astrophysical Quantities (London: Athlone), 134
Baltrusaitis, R. M., et al. 1985a, Nucl. Instr. Meth., A240, 410
Baltrusaitis, R. M., et al. 1985b, Phys. Rev. Lett. 54, 1875
Baltrusaitis, R. M., et al. 1987, J. Phys. G: Nucl. Phys. 13, 115
Bird, D. J., et al. 1993a, Proc. 23rd Int. Cosmic Ray Conf. (Calgary), 2, 38
Bird, D. J., et al. 1993b, Proc. 23rd Int. Cosmic Ray Conf. (Calgary), 2, 51
Bird, D. J., et al. 1993c, Proc. 23rd Int. Cosmic Ray Conf. (Calgary), 2, 55
Bunner, A. N. 1964, Ph.D. thesis, Cornell Univ.
Cassiday, G. L. 1985, Ann. Rev. Nucl. Part. Sci., 35, 321
Dozkhenko, O. I., & Pomanskii, A. A. 1964, Soviet Phys. JETP, 18, 187
DPG Meteorological Group. 1992, private communication
Efimov, N. N., Egorov, T. A., Glushkov, A. V., Pravdin, M. I., & Sleptsov, I. Ye. 1991, in Proc. Int. Symp. on Astrophysical Aspects of the Most Energetic Cosmic Rays, ed. M. Nagano & F. Takahara (Singapore: World Scientific), 20
Elbert, J. W., Stanev, T., & Torii, S. 1983, Proc. 18th Int. Cosmic Ray Conf. (Bangalore), 6, 227
Gaisser, T. K., & Hillas, A. M. 1977, Proc. 15th Int. Cosmic Ray Conf. (Plovdiv), 8, 353
Gaisser, T. K., et al. 1993, Phys. Rev. D, 47, 1919
Greisen, K. 1966, Phys. Rev. Lett., 16, 748
Hartman, P. L. 1968, Planet. Space Sci., 16, 1315
Hill, C. T., & Schramm, D. N. 1985, Phys. Rev. D, 31, 564
Hillas, A. M. 1982, J. Phys. G: Nucl. Phys., 8, 1461
Hughes, R. H. 1985, J. Opt. Soc. Am. B, 2, 362
Kopeliovich, N. N., Nikolaev, N. N., & Potashnikova, I. K. 1989, Phys. Rev. D, 39, 769
Kneizys, F. X., et al. 1988, Users Guide to LOWTRAN 7, AFGL-TR-88-0177, Air Force Geophysics Laboratory
Lawrence, M. A., Reid, R. J. O., & Watson, A. A. 1990, Proc. 21st Int. Cosmic Ray Conf. (Adelaide), 3, 159
Linsley, J. 1983, Proc. 18th Int. Cosmic Ray Conf. (Bangalore), 12, 135
Lloyd-Evans, J. 1991, Proc. 22nd Int. Cosmic Ray Conf. (Dublin), 5, 215
Nagano, M., et al. 1992, J. Phys. G: Nucl. Phys., 18, 423
Penndorf, R. 1957, J. Opt. Soc. Am. 47, 176
Rossi, B. 1952, High Energy Particles (New York: Prentice-Hall), chap. 5
Shettle, E. P., Kneizys, F. X., & Gallery, W. O. 1980, Appl. Opt., 19, 2873
Sokolsky, P. 1990, Proposal to Construct a High Resolution Eye (HiRes) Detector, Appendix D
Sokolsky, P., Sommers, P., & Dawson, B. 1992, Phys. Rep. 217, 227
Stanev, T., et al. 1981, Proc. 17th Int. Cosmic Ray Conf. (Paris), 6, 256
Stecker, F. W. 1989, Nature, 342, 401
Watson, A. A. 1991, in Proc. 12th European Cosmic Ray Symp. (Nottingham), Nucl. Phys. B Suppl. 22B, 116
Yoshida, S., & Teshima, M. 1990, Proc. 21st Int. Cosmic Ray Conf. (Adelaide), 3, 165
Zatsepin, G. T., & Kuzmin, V. A. 1966, Soviet Phys.—JEPT Lett., 4, 78